JOURNAL OF MATERIALS SCIENCE 31 (1996) 1829–1841

Influence of stress intensity and crack speed on fracture surface topography: mirror to mist transition

D. HULL*
Department of Materials Science and Engineering, University of Liverpool, UK

The transition from very smooth "mirror" crack growth to the early stages of roughening associated with "mist" has been investigated using a range of surface topography techniques. The fracture mechanics properties of the brittle, glassy and isotropic epoxy resin used in this work were characterized using compact tension (CT) and double torsion (DT) tests ($K_{\text{Ic}} = 0.65$ MN m$^{-3/2}$). In the DT test, the mist to mirror transition occurred over a large section of the test sample and this facilitated examination by optical microscopy, scanning electron microscopy, atomic force microscopy and non-contact laser profilometry. Measurements on Wallner lines and river lines were used to map the crack velocities and directions over the fracture surface. The transition from mist to mirror, for a decelerating crack, occurred at a crack velocity, $v_c = 0.1 v_t$, where v_t is the shear wave velocity. There was a sharp change in roughness at the transition but no discontinuity in the crack deceleration behaviour. Two main topographical features were observed at the transition: firstly, undulations in the mirror region which decreased in amplitude away from the transition for a decelerating crack and, by implication, vice versa; secondly, a progressive decrease in river line density (for a decelerating crack). Detailed atomic force microscope profilometry was used to determine the surface topography associated with these features. The results provide an insight into the development of crack instabilities under dynamic conditions and a basis for interpreting the progressive development of roughness up to macroscopic bifurcation.

1. Introduction

The terms mirror, mist and hackle have been used for many decades to describe characteristic features on the fracture surfaces of brittle metals, plastics and ceramics: amorphous and crystalline. The work of Johnson and Holloway [1] on the fracture of inorganic glass provides an important starting point. There have been many interpretations of these features which have been associated with various stages of crack growth and some misconceptions have arisen. In many cases the mirror, mist and hackle regions are best described in terms of continuous changes in the conditions of crack growth because the boundaries between them are somewhat arbitrary. However, it is possible to map out boundaries on the fracture surface which have the same degree of roughening and arbitrarily to assign regions of mirror, mist and hackle.

In simple tensile tests of isotropic brittle solids, the mirror, mist and hackle boundaries on cracks which have been nucleated at the surface are approximately semi-circular and the radii of the boundaries, $r(r_{\text{Mirror}}, r_{\text{Mist}}, r_{\text{Hackle}})$, have been shown experimentally to be related to the fracture stress, σ_f, through the relationship

$$\sigma_f r^{1/2} = M \qquad (1)$$

where M is a constant. This equation has the same form as the Griffith equation and M may be interpreted in terms of $(EG_c)^{1/2}$, where E is Young's modulus and G_c is the critical strain energy release rate, or, alternatively, to a critical fracture toughness parameter such as the critical stress intensity factor at the initiation of unstable growth, K_{Ic}, or the dynamic stress intensity factor, K_d. Helpful reviews of this subject, including details of experimental work, are available, see, for example [2–4]. Deviations from semi-circular boundaries arise when the velocity of crack expansion is not independent of direction in the plane of the crack. Differently shaped boundaries have been observed in rectangular and circular section tensile specimens, in circular rods fractured in axial tension compared with bending [5–8], and in single crystals compared with homogeneous isotropic materials [9, 10].

Mirror, mist and hackle result from changes in surface roughness. Thus, explanations for the empirical observations described by Equation 1 must relate

---

* Emeritus Goldsmiths' Professor of Metallurgy, University of Cambridge, UK.

0022–2461

to changes in the micromechanisms of crack growth with the stress fields around the expanding crack and the effective time that the material at the crack tip is under stress. Both these factors depend on the crack velocity and are influenced by secondary effects such as reflected elastic waves. It is important to distinguish between the conditions experienced by an expanding crack and those associated with conventional fracture toughness testing which are concerned with the critical condition for initiating the growth of an unstable crack.

The influence of dynamic stress intensity on crack velocity has been investigated in transparent, brittle, thermosetting and thermoplastic polymers where it is possible experimentally to measure K_d using either caustics or dynamic photoelasticity [11–17]. It has been shown that, initially, the crack velocity, v_c, increases very rapidly for only a small change in K_d and then it levels off as the crack approaches the terminal velocity, which is associated with macroscopic bifurcation. Similar observations were made by Takahashi and Arakawa [18, 19] who also measured the change in surface roughness with K_d and v_c. They found that it was not possible to correlate roughness directly with either K_d or v_c but that there was a linear increase of roughness with $R^* v_c$ where

$$\begin{aligned} R^* &= R_d - R_a \\ &= (K_d^2 - K_a^2)/E_d \qquad (2) \end{aligned}$$

R is the crack extension resistance, subscript d relates to dynamic values and subscript a to the values for an arresting crack. This observation is consistent with the view that both the stress conditions and the crack velocity are important in determining the roughness of the fracture surface.

The nature of roughening is strongly dependent on the microstructure of the material which has a dominant effect on the micromechanisms of deformation and fracture which occur in the region of the tip of the crack. In single-phase crystalline materials, deformation is dominated by dislocation motion to produce slip and twinning. These processes can result in deviation of the crack out of the primary plane of propagation. The micromechanisms are much less well-defined in homogeneous amorphous materials, with the exception of crazing in some amorphous thermoplastics. In multi-phase crystalline and amorphous materials phase boundaries play an important part in the deformation and fracture processes at the crack tip. However, mirror, mist and hackle features are most pronounced in very brittle homogeneous amorphous materials and it is difficult to identify the relevant processes which can be used to explain progressive roughening.

Most of the explanations in the literature, (see, for example [15, 19, 20]) rely on the proposal made by Congleton and Petch [21] that Griffith cracks are nucleated in the high-stress regions ahead of the crack. These microcracks then interact with the main crack and "escape" out of the plane of the main crack by micro-bifurcation or crack-branching because of changes in the distribution of stresses around the rapidly expanding crack [22, 23]. There are many difficulties with this approach: (i) there is no convincing evidence for the initiation of microcracks ahead of the crack tip in brittle homogeneous inorganic and organic glasses which do not craze, (ii) because the roughness develops progressively, and in the early stage of mist is extremely fine [24], the distribution of Griffith flaws must be on a very fine scale, and (iii) the stresses required to activate very small flaws close to the crack tip will approach the theoretical strength of the material and it is difficult to envisage why a growing crack should expand by microcrack initiation rather than by bond breakage at the tip.

In this paper, and its companion [25], we are concerned with the progressive development of roughening with K_d and v_t in an amorphous brittle epoxy resin. It has been found in the present work that the sequence of events associated with increased roughening during crack acceleration is closely similar to that which occurs during the reduced roughening as the crack decelerates. This point is dealt with in more detail in the second paper; for ease of description and presentation we concentrate on the deceleration stage in this first paper. The changes associated with the full range of roughening up to macroscopic bifurcation are also treated in the second paper. The first paper is concerned primarily with the changes which occur in the early stages of roughening from mirror to mist and the second paper with the changes which occur from mist to hackle and full-scale bifurcation. By choice of test geometry it has been possible to extend the regions over which the transitions occur and so facilitate experimental observations. Similarly, it has been possible to investigate the transitions for accelerating and decelerating cracks.

The experimental methods are described in the next section of this paper and this is followed by an explanatory section which gives information to characterize the fracture behaviour of the epoxy resin used in this work in relation to factors such as crack tip blunting, plastic zone size, critical stress intensity factors, stable and unstable growth conditions, etc. This is important because we must distinguish between fracture surfaces generated under different conditions. There follows a general introduction to the main observations which were made on the fracture surface and a section which describes the application of the Wallner line approach for measuring crack velocities in very smooth regions of fracture. This provides a "bench-mark" for determining crack velocities elsewhere on the fracture surface using crack trajectories in double torsion specimens. Measurements of roughness and microscopic observations of changes in surface topography are described in the next section. In the last section some new ideas about the mechanisms involved in the initial stages of roughening, based on the experimental observations, are presented.

2. Experimental procedure

2.1. Material

As in previous work [26], a Ciba Geigy Araldite LY 1927 epoxy resin was used. This is a cold-curing

TABLE I Properties of post-cured epoxy resin at 20 °C

Modulus, E (GPa)	3.1
Poisson's ratio, ν	0.40
Tensile strength (brittle fracture), σ^* (MPa)	70
Elongation to fracture in tension, ε^* (%)	3.8
Fracture toughness, K_{Ic}, (MN m$^{-3/2}$)	0.65
Density, (10^3 kg m^{-3})	1.16

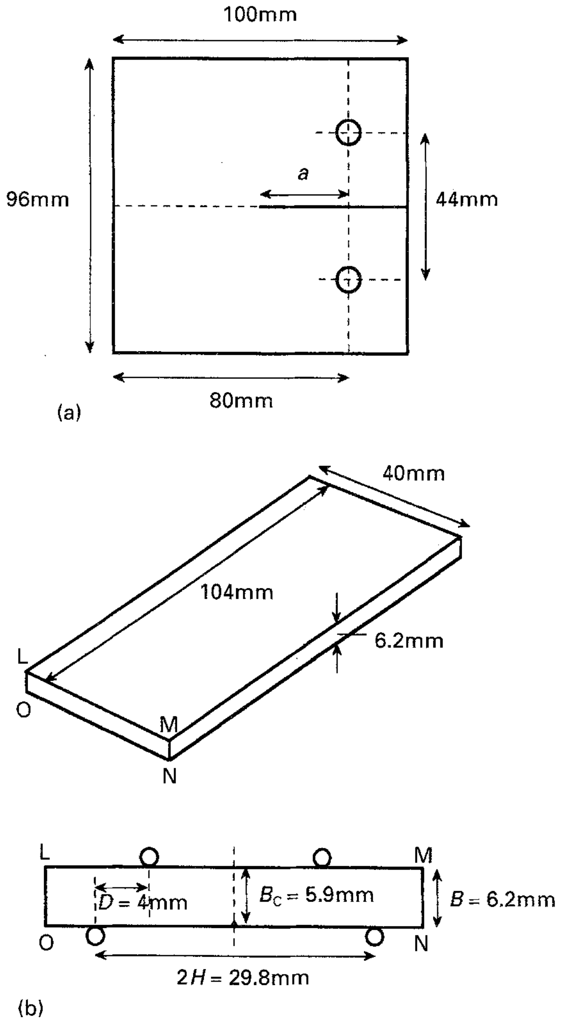

Figure 1 Geometry and dimensions of the test specimens: (a) compact tension (CT), plate thickness 6.2 mm; (b) double torsion (DT).

low-viscosity bismaleidmide resin which was mixed with hardener Araldite HY 1927 in proportions 100:36 by weight. The resin was cured at 20 °C for 24 h and post-cured at 100 °C for 4 h. Plates about 6 mm thick were produced by casting into glass-sided moulds and the plates were cut into test samples using a diamond-impregnated cutting wheel. The properties of the resin are summarised in Table I.

2.2. Test methods

The two main mechanical test methods and the dimensions of the test specimens are illustrated in Fig. 1. The methods are based on configurations, reported in the literature, which have been used for evaluating the fracture properties of brittle polymers under pure mode I loading conditions. The compact tension (CT) test shown in Fig. 1a was used to determine K_{Ic} and it provided additional information about the "stick–slip" behaviour of crack extension. The dimensions of the specimens were based on those used by Kinloch *et al.* [27]. K_{Ic} was calculated from [28]

$$K_{Ic} = (P_Q/HW^{1/2})f(a/W) \tag{3a}$$

where P_Q is the load at crack initiation, H is the thickness of the test sheet, a and W are as illustrated in Fig. 1a, and $f(a/W)$ is given by

$$f(a/W) = \frac{(2 + a/W)(0.886 + 4.64a/W - 13.32a^2/W^2 + 14.72a^3/W^3 - 5.6a^4/W^4)}{(1 - a/W)^{3/2}} \tag{3b}$$

By suitable choice of a the test satisfies the procedures prescribed by ASTM (E399-83) [28] for valid K_{Ic} values.

The double torsion (DT) test, illustrated in Fig. 1b, has been used extensively in the past to follow crack growth under stable conditions. The interpretation of the test data is difficult because of the complex stress distribution and the geometry of the crack front (see, for example, Leevers [29] and Stalder and Kausch [30]). In particular, the crack velocity is strongly dependent on the instantaneous orientation of the crack front. The test geometry, shown in Fig. 1b, was similar to that described by Leevers [29]. Following Leevers, K_{Ic} for plane strain, is given by

$$K_{Ic} = \left(\frac{EG_c}{(1 - \nu^2)}\right)^{1/2} = \left(\frac{E}{(1 - \nu^2)2B_c}\frac{P_c^2}{E}\frac{(1 + \nu)}{}\frac{D^2}{ZHB^3}\right)^{1/2} \tag{4}$$

The dimensions D, H, B and B_c are illustrated in Fig. 1b, ν is Poisson's ratio, P_c is the fracture load and Z is a constant which depends on (H/B) tending to 1/3 as this ratio becomes large. An important characteristic of the DT test is that, for stable crack growth at constant speed, K_I is independent of crack length.

All the mechanical tests were made in a Schenck Universal testing machine at 20 ± 2 °C. The crosshead speed for CT tests was 0.5 mm min^{-1} and for the DT tests it was 5 mm min^{-1}. Sharp starter cracks were introduced by controlled impact of a razor blade.

2.3. Roughness measurements

The roughness of the fracture surfaces was determined using two types of profilometer which give different effective resolutions and scan differently sized areas of the surface. The Rodenstock Profilometer is a non-contact instrument which uses a laser with a 1 μm spot size. It was used to scan large areas of the fracture surface. The Nanoscope® III Atomic Force Microscope (AFM) is essentially a contact profilometer which can be used to generate three-dimensional images of the surface at high resolution. The effective stylus tip radius was about 30 nm with a nominal tip height of 3 µm and a tip cone angle of 70 °. At any location on the surface the maximum scanned area was 150 µm × 150 µm. To cover larger areas of the fracture surface successive images of adjacent areas were scanned to form a collage.

Both these instruments have sophisticated data analysis capabilities which can provide a wide range of roughness parameters. For the purpose of the present investigation, the data are presented in terms of the root mean square of roughness, R_q, defined by

$$R_q = \left[\frac{1}{L}\int_0^L |f(x)|^2\,\mathrm{d}x\right]^{1/2} \qquad (5)$$

where L is the scanned length and $f(x)$ is the measured height of the surface at point x. To remove the effects of long-term waviness of the roughness profile, the Rodenstock profilometer data was filtered to cut-off lengths less than 15% of the scanned length. Because of the large differences in the characteristics of these two approaches to profile measurements, no attempt has been made to relate the R_q values of the different tests. Details of the regions which were scanned are given later.

2.4. Microscopy

The fracture surfaces were examined using a Nikon Optiphot optical microscope with combined reflected and transmitted light to obtain optimum contrast effects. A Hitachi SN2460 scanning electron microscope (SEM) was used to obtain more detail of the surface topography. Before examination in the SEM, the fracture surfaces were sputter coated with gold–palladium. Low operating voltages were used to give low penetration of electrons and so enhance the topographical features on relatively smooth surfaces. High-resolution studies of the topography were made with the AFM mentioned above. Both continuous scanning and tapping modes were used to obtain optimum resolution.

3. Characterization of fracture properties of epoxy resin

The CT test geometry specimens were used to determine the static fracture properties of the epoxy resin. A typical load–displacement trace is shown in Fig. 2a. Unstable crack growth was initiated at $P_{\max}$ and fracture occurred in a series of stick–slip movements. The loads at crack arrest, P_a, and crack re-initiation, P_i, were determined from the load–displacement traces and the corresponding crack lengths were measured directly from the fracture surfaces from the position of the arrest marks. The crack fronts were curved and the mean position was used for calculation purposes. Data from two tests are shown in Table II. Two values of K_{Ic} are quoted. $K_{Ic(i)}$ is the critical stress intensity for the start of unstable crack propagation. Under the loading conditions in this test the crack at first accelerates and the load relaxes so the stress intensity decreases and the crack stops. $K_{Ic(a)}$ is the stress intensity at crack arrest calculated from the load when the crack stops, and the new crack length. Successive stick–slip growth resulted in a number of values of $K_{Ic(i)}$ and $K_{Ic(a)}$. The difference between $K_{Ic(i)}$ and $K_{Ic(a)}$ is indicative of some crack tip blunting before unstable crack growth. Fractographic examination showed that a small amount of stable crack growth preceded unstable growth. The ratio $K_{Ic(i)}/K_{Ic(a)}$ is an indication of the extent of blunting [31]. A measure of blunting can be obtained also from the

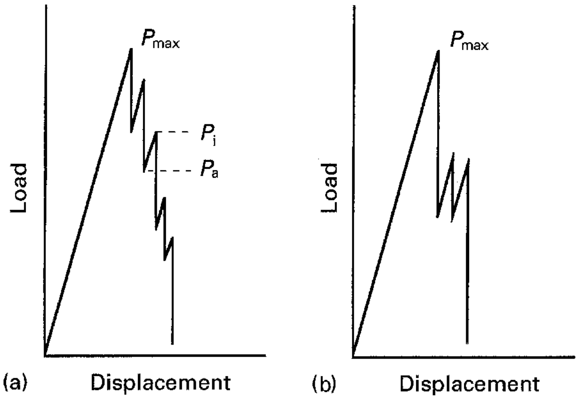

Figure 2 Typical load–displacement traces: (a) compact tension, (b) double torsion.

TABLE II Summary of data from CT tests

Specimen	a/W	$f(a/W)$	$K_{Ic(i)}$ ($MN\,m^{-3/2}$)	$K_{Ic(a)}$ ($MN\,m^{-3/2}$)	$K_{Ic(i)}/K_{Ic(a)}$
1	0.167	3.8581	0.622		
	0.351	6.4083	0.645	0.551	1.17
	0.492	9.4260	0.650	0.529	1.23
	0.673	18.7814	0.612	0.481	1.27
2	0.251	4.9381	0.520		
	0.287	5.4340	0.613	0.512	1.20
	0.410	7.4747	0.640	0.528	1.21
	0.579	12.6041	0.642	0.511	1.26

expression for crack tip opening displacement (COD)

$$\delta_t = \frac{4}{\pi}\frac{K_{Ic}^2}{E\sigma_{ys}} \tag{6}$$

Taking $\sigma_{ys} = 100$ MPa, $K_{Ic} = 0.65$ MN m$^{-3/2}$ and $E = 3.1$ GPa gives $\delta_t = 1.7$ μm.

The DT test geometry can be used also to determine K_{Ic} and, under stick–slip conditions, two values ($K_{Ic(i)}$ and $K_{Ic(a)}$) are obtained [31]. There are difficulties in interpreting the data because the shape of the expanding crack front in this test means that the crack velocity varies around the front [29]. In the present work, the test was used to produce a fracture surface with an extended region over which an initially unstable crack decelerated. The approach is illustrated in Fig. 2b which shows a typical load–displacement trace. When a relatively blunt notch is used as the crack starter the stress intensity at the initiation of unstable cracking is larger than K_{Ic} so that subsequent crack growth occurs at an initially higher value than that required for propagation from a sharp crack. Eventually the stresses in the specimen are relaxed and the crack slows down and stops. For the results described in the next section the initial stress intensity was 0.96 MN m$^{-3/2}$ and the first crack extended over about 70 mm before stopping. Further propagation occurred by stick–slip and, in agreement with the CT results in Table II, $K_{Ic(i)}/K_{Ic(a)}$ was about 1.2.

4. Mist to mirror transition: general observations

A schematic representation of the fracture surface of the DT specimen fractured under the conditions described in Section 3 is shown in Fig. 3. The top edge of the specimen was grooved with a notch, 0.8 mm deep, to control the direction of crack growth. The crack nucleated at N and the main crack front expanded in the direction indicated. One crack arrest occurred and the position is shown by the crack arrest line. The curvature of the crack front at arrest gives an indication of the instantaneous shape of the moving crack from which it follows that the local direction of crack movement and the crack velocity varied along the crack front.

The majority of the surface was mirror smooth but a region of mist occurred close to the top surface and there was also some mist around the crack arrest line. The width of the mist region was approximately constant over the length marked A–A′. Optical microscopy indicated that the appearance of the fracture surface across the width in this region was independent of position. This means that the conditions of crack growth were approximately constant in this region. To facilitate more detailed examination, the specimen was cut into shorter lengths which were used for optical, SEM and AFM studies and for Rodenstock surface roughness measurements as indicated in Fig. 3.

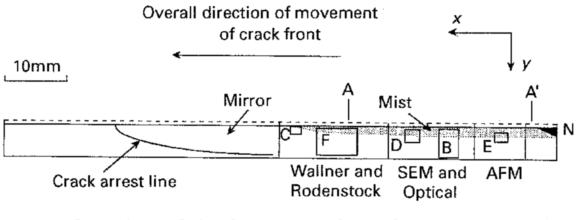

Figure 3 Overview of the fracture surface of a DT test specimen showing the distribution of mist and mirror and the position of sections used for optical microscopy, SEM, AFM and Rodenstock profilometry.

Figure 4 Collage of optical micrographs of the fracture surface across the thickness of a DT specimen (area B in Fig. 3) showing mist to mirror transition and Wallner lines.

The appearance of the fracture surface is illustrated in Fig. 4 with a collage of optical micrographs from area B in Fig. 3. The transition from mist to mirror occurs over a short distance. In the mirror region there were a few approximately equally spaced residual river lines which can be used to map out the direction of crack growth at all points on the surface.

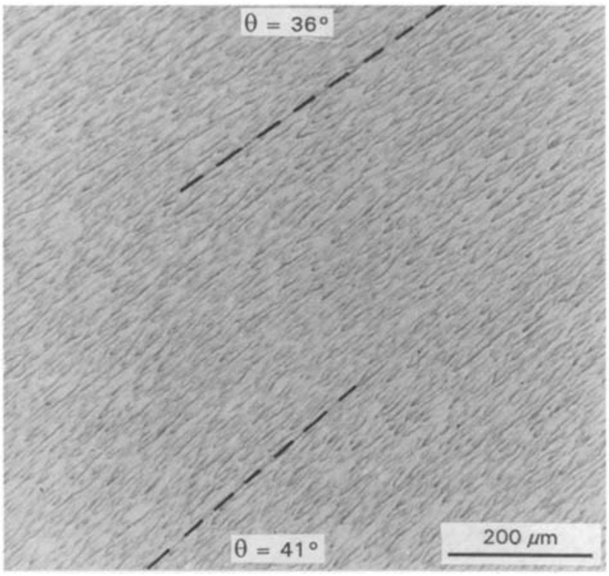

Figure 5 Optical micrograph of part of the mist region to illustrate the method of determining the local direction of crack propagation. θ is the angle between the crack propagation direction and x-axis.

Thus, the orientation of the river line at any point P in Fig. 4 defines vector f_2 parallel to the direction of crack propagation and vector f_3 tangential to the crack tip at that point [32]. Clearly, the local direction of crack growth changes across the width of the specimen.

The direction of growth in the mist region was obtained from higher magnification optical micrographs, see, for example, Fig. 5. The fine detail of the fracture surface in this region is considered in more detail in the second paper. Using this approach, the direction of crack growth across the complete area B (Fig. 3) was obtained by mapping the local directions sequentially. This is represented graphically in Fig. 6a. Over the region A–A′ (Fig. 3) the shape of the crack direction curve was almost independent of position along the specimen in the x-direction. This is illustrated in Fig. 6b which demonstrates that the corresponding shape of the crack front is also independent of position. It follows that the ratio of crack velocities is given by

$$v_{(y_1)}/v_{(y_2)} = v_{(\theta_1)}/v_{(\theta_2)} = \cos\theta_1/\cos\theta_2 \qquad (7)$$

where θ is the angle between the direction of movement of the crack front as a whole (x-axis) and f_2. The variation of $v_{(\theta=0)}/v_{(\theta)}$ obtained from the same experimental data used to produce Fig. 6a is shown in Fig. 7. In this case the velocity is plotted against the distance the crack has travelled along the profile shown in Fig. 6a. The position of the boundary of the mist to mirror transition region is shown by the shaded region in Fig. 7. There are no discontinuities at the transition in either the crack growth direction curve or the crack velocity curve.

In addition to the river lines in the mirror region of Fig. 4 there are a series of Wallner lines [33] produced by the interaction of shear waves with the crack front.

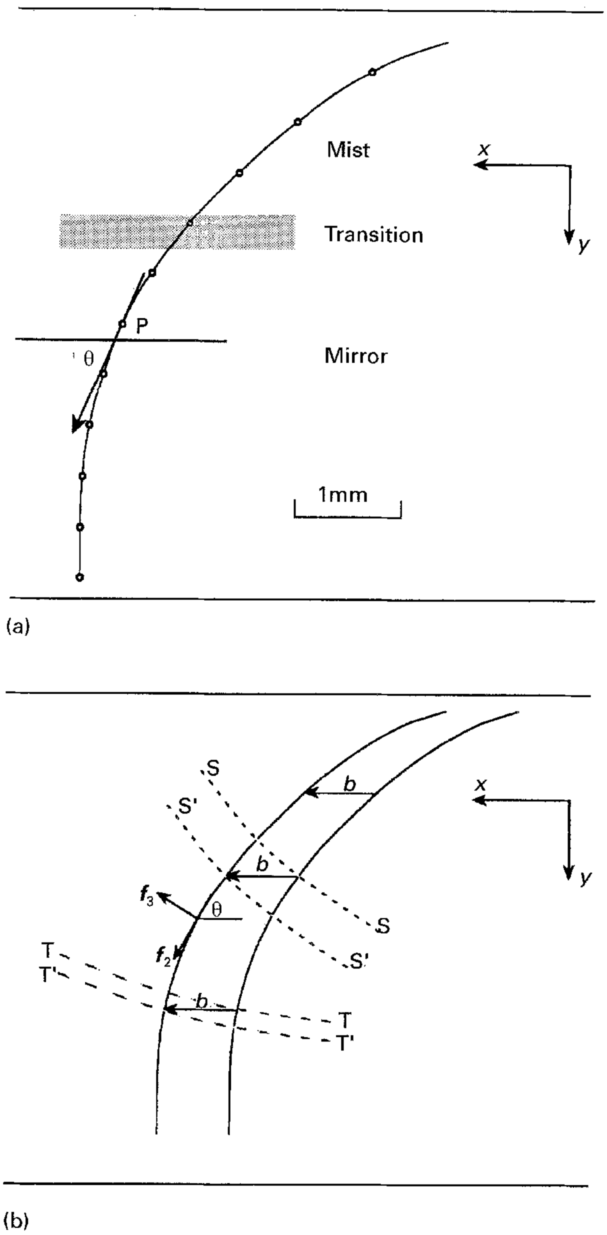

Figure 6 Direction of crack propagation in a DT specimen: (a) experimentally determined direction across the width of the specimen, the position of mist to mirror transition is indicated by the shaded region, (b) schematic representation of two positions of a crack front moving at a constant speed in the x-direction, the crack front S–S moves to S′–S′ and the crack front T–T moves to T′–T′ for a crack front displacement b in the x-direction.

Following Smekal [34] it is possible to determine the crack velocity from the shape of the Wallner lines provided that the source of the shear wave and the direction of crack propagation are known (see, for example [9, 35]). This method was used to obtain a measure of the local crack velocity in section C (Fig. 3) and is described in more detail in the next section.

The fine detail of the surface topography, with particular reference to the mist to mirror transition, was investigated using SEM and AFM. The areas examined were from D and E (Fig. 3); the detailed results are described in Section 6.

Finally, Rodenstock non-contact profilometry was used to measure the change of roughness across the mist to mirror transition. The sample used and the

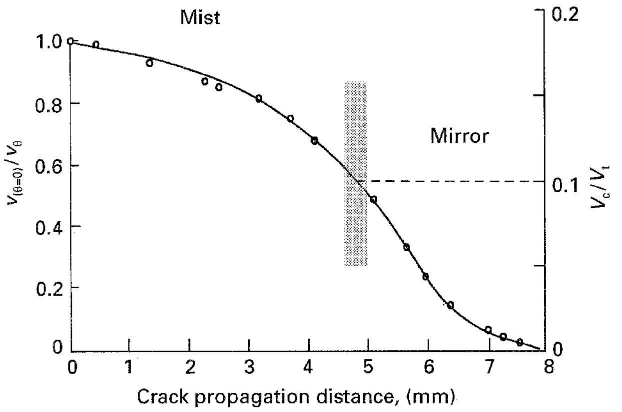

Figure 7 Variation of crack velocity with crack propagation distance in a DT specimen. Experimental points refer to measurements of $v_{(\theta=0)}/v_\theta$ based on the data of Fig. 6. The v_c/v_t scale was based on experimental observation that $v_c/v_t = 0.10$ at mist to mirror transition.

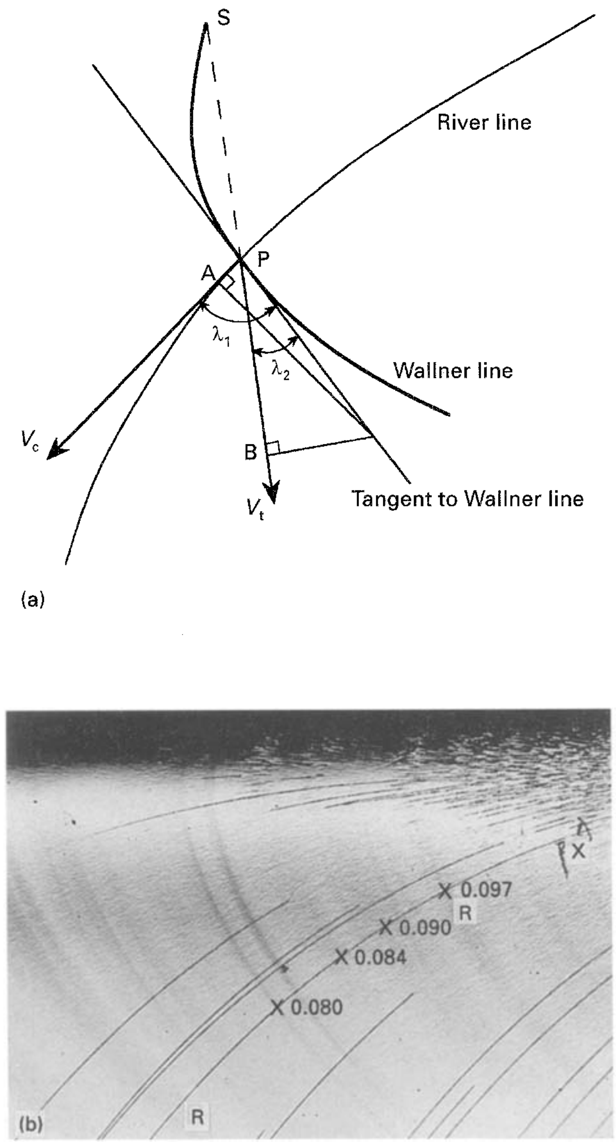

Figure 8 Determination of the crack velocity from Wallner line measurements: (a) method of analysis, (b) optical micrograph of area C (Fig. 3) showing Wallner lines and river lines.

position of the roughness traces is marked F in Fig. 3, and the detailed results are given in Section 6.

5. Mapping of crack velocities

The method used to determine the crack velocity from Wallner line traces is illustrated in Fig. 8a. At any point P on a Wallner line, initiated at S, the directions of crack propagation and expanding shear wave, velocities v_c and v_t, respectively, are as shown. Since $PA = v_c\Delta t$ and $PB = v_t\Delta t$, it follows that

$$\frac{v_c}{v_t} = \frac{PA}{PB}$$

$$= \frac{\cos\lambda_1}{\cos\lambda_2} \tag{8}$$

The sources of the Wallner lines in Fig. 4 are not clear so that it was not possible to determine the crack velocity in this region of the fracture surface using this approach directly. However, in area C (Fig. 3) of the fracture surface, the mirror region extended to the top surface of the test specimen and it was possible to identify the origin of the Wallner lines with some accuracy. An optical micrograph of area C is shown in Fig. 8b. A series of Wallner lines interact with a few residual river lines. At any point on the river line the local direction of crack propagation can be determined from the tangent at that point. The values of λ_1 and λ_2 were determined at a number of positions along river line RR using graphical methods. The velocity ratio, v_c/v_t, was calculated from Equation 8 and the results are recorded on Fig. 8b.

The ratio v_c/v_t decreased towards the mist to mirror transition region. The value of v_c/v_t at the transition (X in Fig. 8b) was determined using the approach described in Section 4 assuming that the overall crack front was travelling at constant speed. Thus, the ratio of velocities at any two points on the same river line is given by Equation 7. Using the values of v_c/v_t shown on Fig. 8b the values of v_c/v_t at the transition were 0.102, 0.099, 0.102 and 0.106. A value of 0.10 is used in the remainder of the paper. The mechanical properties of the epoxy resin used in this work are closely similar to those of Araldite D quoted by Arakawa and Takahashi [19]. Thus, using their value, $v_t = 1170\ \mathrm{m\,s^{-1}}$, the crack velocity at the transition was about $120\ \mathrm{m\,s^{-1}}$.

Assuming that v_c/v_t at the mist to mirror transition is constant, $v_c/v_t = 0.10$, the velocity profile across the full section of the specimen (see Fig. 4), was determined. This is illustrated in Fig. 7. The crack velocity close to the top surface was about $0.18v_t$ and at the bottom surface it approached zero. (Note, in a similar experiment, using the compact tension test geometry of Arakawa and Takahashi [19], which is described in the second paper, the velocity of crack propagation at the mirror to mist transition for an accelerating crack was measured from Wallner lines, and it was found that $v_c/v_t = 0.115$, slightly above the result reported above for a decelerating crack.)

6. Topographical changes in the transition region

The Rodenstock non-contact laser profilometer was used to measure the roughness in area F (Fig. 3). An enlarged diagram of this section is shown in Fig. 9a. Ten roughness traces 6 mm long were made in a 4 mm wide band which spanned the transition region. The results in Fig. 9b show examples of the traces and in Fig. 9c the R_q values have been plotted in the y-direction. As illustrated in Fig. 9a, trace 1 was completely in the mist region and trace 4 was completely in the mirror region. Trace 2, which spanned the transition at an angle of about 45° to the local direction of crack propagation, shows the change in roughness associated with the transition. The R_q values in Fig. 9c indicate that the roughness changed significantly in the transition region and was constant in the mirror region away from the transition. There is a one-to-one correlation between the serrations on the roughness profiles and the residual river lines in the mirror region.

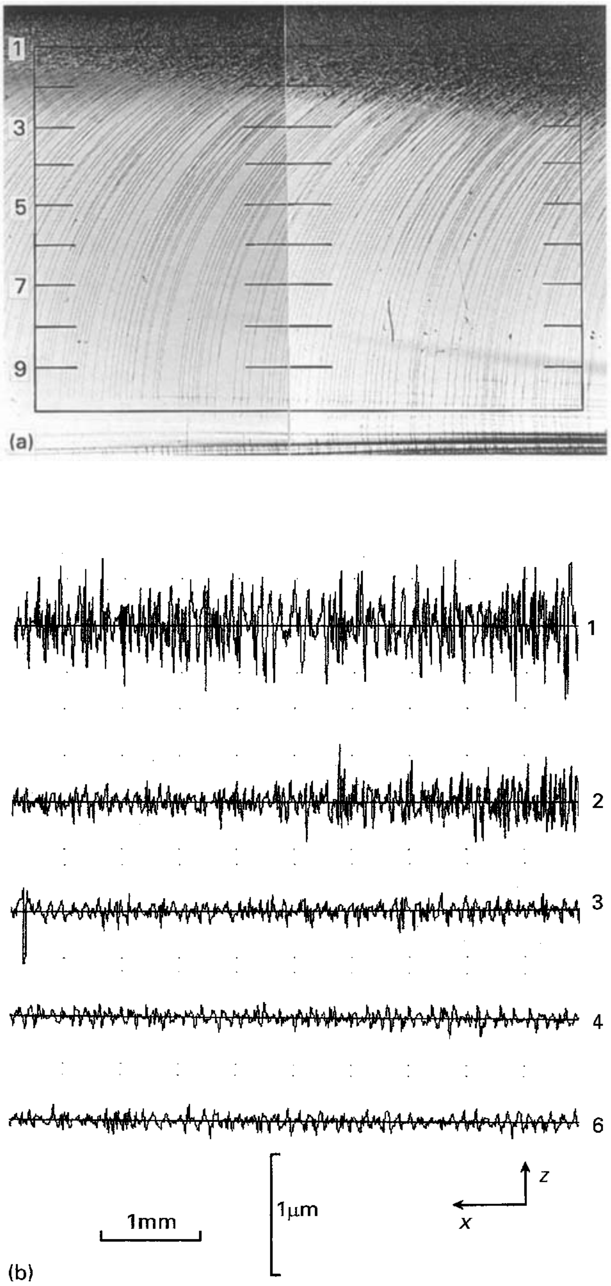

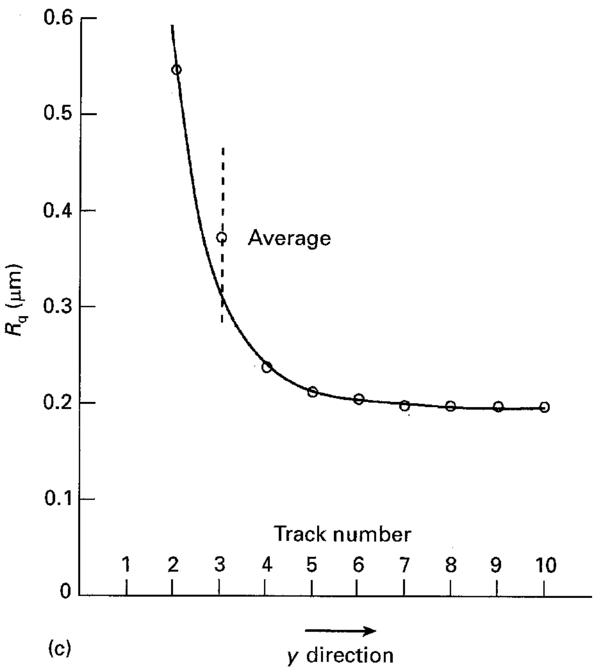

Figure 9 Rodenstock non-contact laser profilometer observations: (a) optical micrograph of a 4 mm × 6 mm area F in Fig. 3 showing the mist to mirror boundary and the position of the roughness traces 1–10; (b) examples of roughness traces, note the different scales of x and z; (c) R_q values across section F in the y-direction.

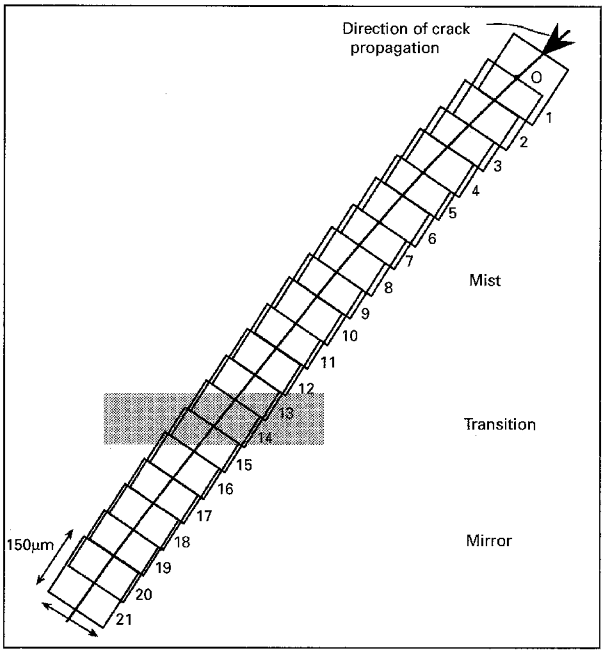

Figure 10 Orientation and position of scans used to investigate topographical details of area E (Fig. 3) using AFM.

The AFM roughness measurements were made with a series of 21 scans 150 μm × 150 μm in area E (Fig. 3). This covered the transition region as illustrated in Fig. 10. In scan 21, the scanning direction was approximately normal to the local direction of crack propagation (i.e. the river line direction) and each 150 μm × 150 μm scan overlapped the next by 75 μm. The scans were used to produce topographical images of the surface and values of R_q.

The values of R_q, averaged over each 150 μm × 150 μm scan, are shown in Fig. 11. The distance was

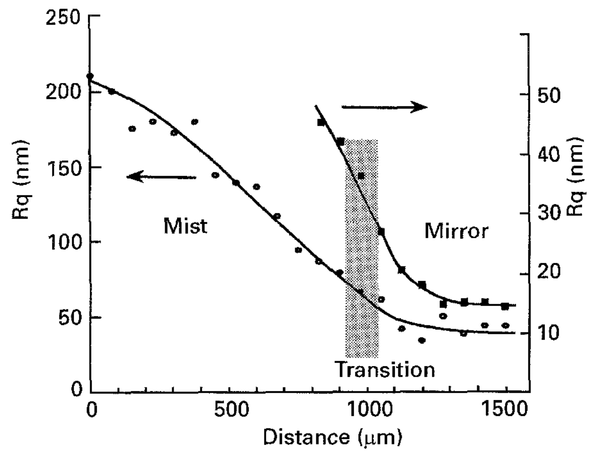

Figure 11 Variation of R_q across the mist to mirror transition determined by AFM; (○) from full-scale 150 μm × 150 μm scans, (■) from line scans about 30 μm long between river line steps and normal to them (see, for example, Fig. 14).

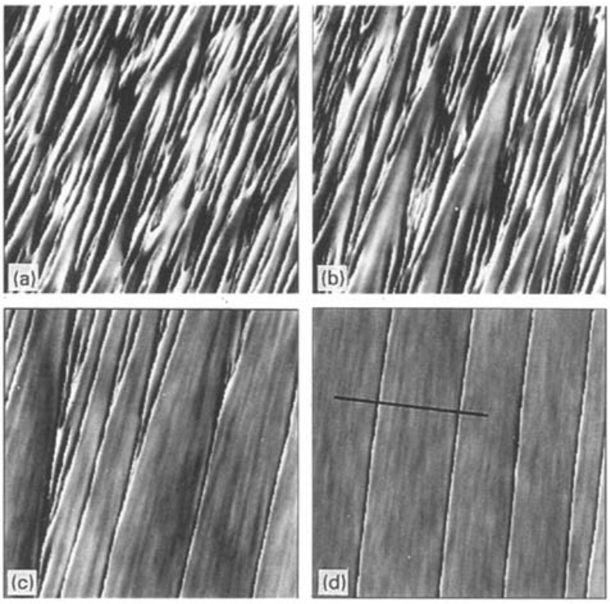

Figure 12 Some typical surface view topographical images obtained by AFM: (a) scan 3, (b) scan 8, (c) scan 14, (d) scan 19, see Fig. 10 for details of positions of these scans. Each scan is 150 μm × 150 μm. The roughness profile along the line in (d) is shown in Fig. 14.

measured along the direction of crack propagation from point O shown in Fig. 10. The measurements, which extended over a crack-growth distance of 1.5 mm, show that R_q decreased progressively from point O in the mist to the mirror region and then levelled off (cf. Fig. 9c). Examples of the topographical images, derived from the same data as the roughness measurements, are shown in Fig. 12. In the mist region (scans 3 and 8, Fig. 12a and b) the surface consisted of a series of steps of opposite sign parallel to the direction of crack propagation which merged together, cancelled each other out and reformed. This aspect is covered in more detail in the second paper. As the mirror region was approached, the rate of nucleation of new steps decreased but merging continued so that the overall density of steps decreased (cf. Fig. 12a and b). At the transition (scan 14, Fig. 12c), merging of the steps was completed and only a few isolated residual river lines, all of the same sign, remained in the mirror region (scan 19, Fig. 12d).

The AFM observations were confirmed by an SEM investigation of a similar region of the surface, i.e. section D in Fig. 3. The results are shown in Fig. 13. The position of the photographs in relation to the transition can be determined from the angle θ between the river lines and the x-axis (cf. Fig. 6). These have been marked on the photographs. The most important features in these photographs are the undulations which occur between the river line steps which are best displayed in Fig. 13c taken in the transition region. The undulations between the steps are irregular and lie parallel to the steps. They are less pronounced in the mirror region away from the transition (Fig. 13d) and are clearly visible between the more closely spaced steps in the mist region (Fig. 13a and b). The undulations were also evident in the optical micrographs (see Fig. 4) but it was difficult to resolve the detail because of the poor contrast.

AFM was used to measure the roughness between the steps and also to determine the topography of the steps. An example is illustrated in Fig. 14. The section profile along the line marked on Fig. 12d is shown in Fig. 14a. The roughness, R_q, over the full length of the scan was 47 nm. The profile crosses two river line steps and these dominate the roughness. The roughness between the steps was measured by locating the two marker arrows along the profile line in the positions illustrated by R–R in Fig. 14a. In this example, R_q between R–R was 14.7 nm. Values of R_q between the steps were measured on scans 12–21 (Fig. 10) across the transition and the results are plotted on Fig. 11. The decrease in R_q at the transition extends into the mirror region. The profile trace in Fig. 14a exaggerates the apparent roughness because different scales are used. In Fig. 14b, the profile in Fig. 14a is shown with the same scales.

An indication of the three-dimensional character of the roughness was obtained by manipulation of the AFM data. Two examples are shown in Fig. 15. Fig. 15a is the same field of view as Fig. 12b taken in the mist region. It shows the data presented as a smoothed three-dimensional image with highly exaggerated peaks and troughs which lie parallel to the local direction of crack propagation. Fig. 15b is a set of line scan profiles of scan 11 (Fig. 10), close to the transition. Each of the profiles illustrates the roughness between the steps and the sequence of profiles shows that there are longer wavelength undulations in the direction of crack propagation in addition to the undulations normal to the direction of crack propagation.

7. Discussion and conclusion

The roughness of fracture surfaces is dependent on many factors, including stress fields, microstructure and material properties. In the interpretation of fracture surface features it is important to distinguish the origin of the effects observed. By choosing a brittle, homogeneous and isotropic organic glass for the present work, many of the important potential variables

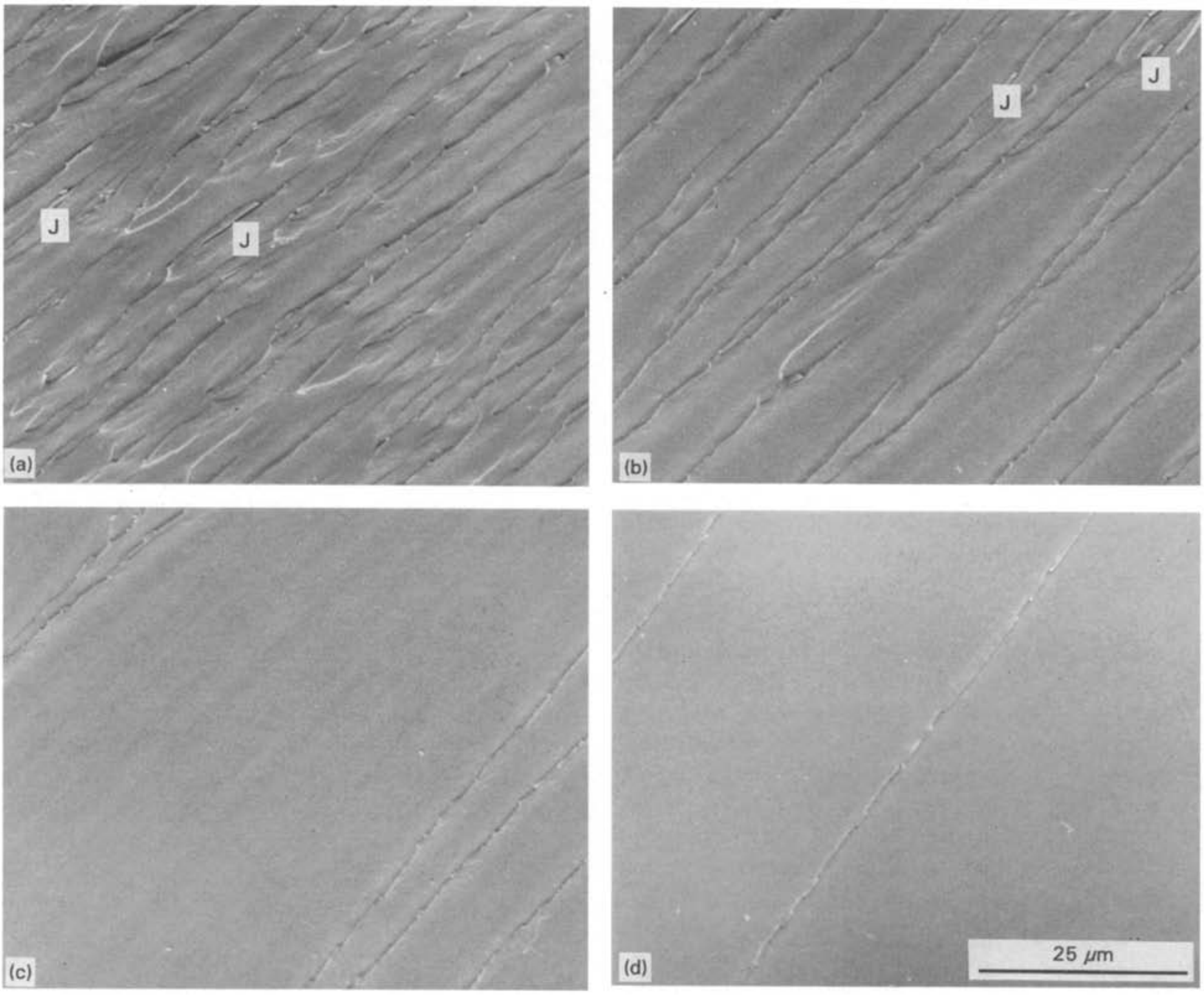

Figure 13 Scanning electron micrographs from area D (Fig. 3) at different values of θ: (a) $\theta = 41°$, (b) $\theta = 47°$, (c) $\theta = 50°$, (d) $\theta = 54°$.

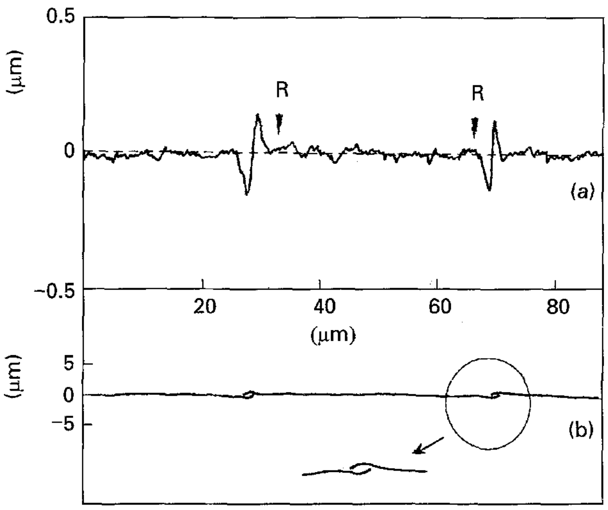

Figure 14 Illustration of the method of obtaining values of R_q from regions between river lines using the AFM image in Fig. 12d: (a) roughness profile of the line marked in Fig. 12d with different magnification scales; (b) the same roughness profile as (a) with the same magnification scales, showing the geometry of river line steps with overlapping cracks, producing isolated prismatic-shaped filaments.

were eliminated and attention was focused on the influence of stress fields. Here one can envisage two fundamentally different reasons for surface roughness. Firstly, roughness results from mixed-mode conditions, which occurs when a mode I crack moves into a mixed mode I/III field [36, 37]. In this case the roughness is caused by the inability of cracks in brittle solids to twist [32] and a series of river line steps is produced. The pattern of steps which merge to form arrays characteristic of a river delta has been known for many decades and is now the subject of some topological analyses, including fractal analysis [38]. However, great care is required to avoid making inaccurate conclusions [39].

The second source of roughness occurs when a mode I crack grows with an increasing K_I stress field. It is this condition which usually applies to work on mirror, mist and hackle, although there has undoubtedly been confusion in the literature when more complex stress fields have occurred in poorly characterized tests. This paper is concerned with the mirror to mist transition for accelerating cracks and the mist to mirror transition for decelerating cracks.

The results show that in the DT test the crack velocity varies continuously along the crack front. At the mist to mirror boundary $v_c/v_t = 0.10$, and there is a distinct change in the fracture surface topography. The residual river lines in the mirror region observed in this work are almost certainly an artefact of the test and are caused by a very small amount of mode III loading, superimposed on the mode I, because the

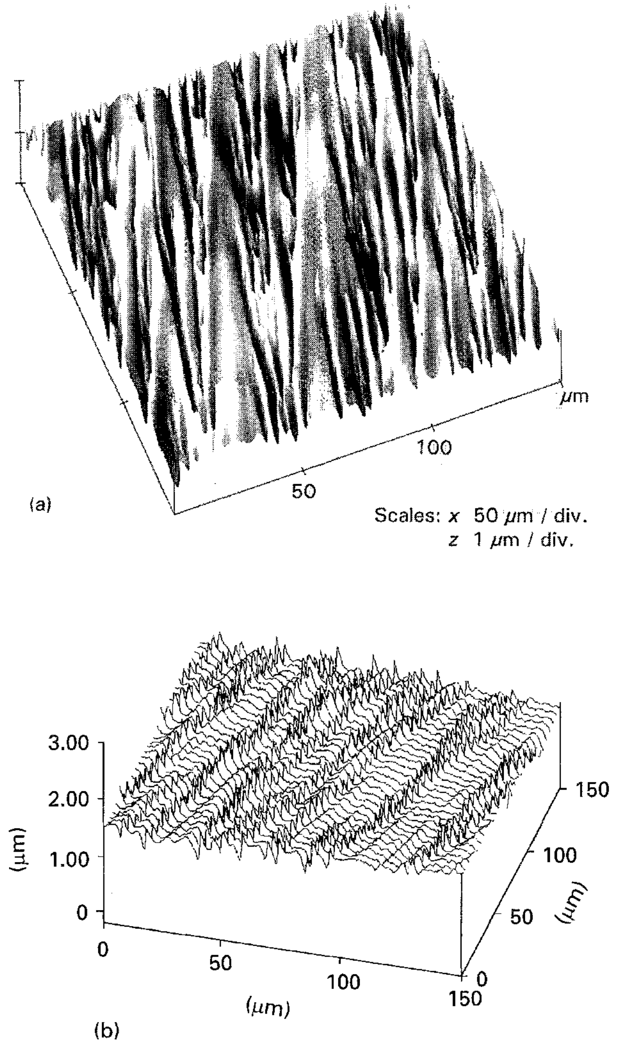

Figure 15 AFM images: (a) perspective image of the same field as scan 8 in Fig. 12; (b) sequential line scan image from scan 11 in Fig. 10.

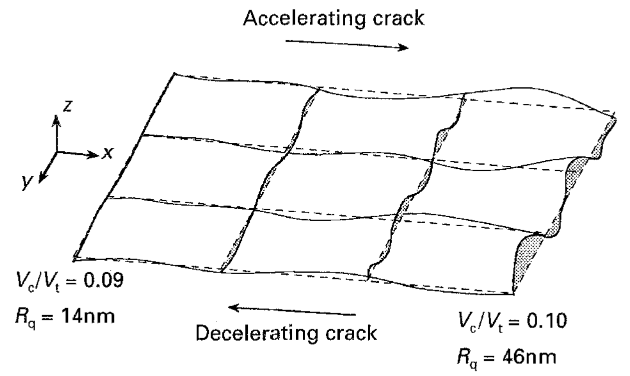

Figure 16 Schematic representation of the increase in amplitude of random undulations on the fracture surface at the mirror to mist transition, leading to nucleation of river line steps.

alignment of the specimen was not absolutely perfect. The geometry of the steps illustrated by the results in Fig. 15b is the same as that observed in more macroscopic tests in which a mode I crack moves into a mixed I/III field [36, 37, 40]. Very fine filaments of material are formed on the fracture surface parallel to the steps (see, for example, J in Fig. 13).

Although the transition has been related to a critical velocity it is debatable, as mentioned in Section 1, whether or not crack velocity or dynamic stress intensity, K_d, is the critical parameter determining the transition and the development of roughness. We return to this point in the second paper [25].

There are two main features associated with the increase in roughness at the transition from mirror to mist (note, it is assumed in this discussion that the sequence is the reverse of that which occurs during crack deceleration; there is ample experimental evidence for this). Firstly, there is a rapid increase in the amplitude of the surface undulations (see Figs 11–13) as illustrated schematically in Fig. 16. The random nature of the undulations, observed in optical microscopy, SEM and AFM, makes a precise description impossible but the main features, shown in Fig. 16, are the short wavelength undulations normal to the direction of crack growth and the relatively long wavelength undulations parallel to the direction of crack growth. It seems likely that the periodicity of the undulations in the x-direction will depend on the rate of change of v_c or K_d with distance. In the DT test this is relatively small compared with a simple tensile test. For a crack propagating at a constant velocity close to the transition velocity, the wavelength in the direction of crack propagation may be very long.

The second main feature is the nucleation of river line steps, which leads to a much larger increase in roughness (Fig. 11). As will be shown in more detail in the second paper, the river line steps are of the same form as the steps produced by a change from mode I to mixed mode I/III with the fundamentally important difference that the steps are randomly formed of opposite sign so that there is no overall rotation of the plane of the crack.

The steps nucleate between existing steps and combine to reinforce or eliminate each other. The rate of nucleation or annihilation depends on whether or not the crack is accelerating or decelerating. The nucleation of the steps is closely related to the undulations. The exact mechanism is obscure and to make even the simplest of speculations we require some model or description of the crack tip.

The K_{Ic} data in Section 3 indicate that the critical crack opening displacement for the material used in this work is about 2 μm. This may be interpreted as the opening at the crack tip immediately before the crack starts to propagate. This dimension is significantly greater than the roughness parameters illustrated in Fig. 11 but it has little relevance to the geometry of a crack propagating at $v_c/v_t = 0.10$ or $v_c = 120\,\mathrm{m\,s^{-1}}$. Some idea of the crack tip opening under such conditions is evident from the observations of filament formation (Sommer's lances [36]) at river line steps (see Figs 13 and 14) which requires the interaction of two non-coplanar cracks less than 200 nm apart. Here the crack opening displacement must be significantly less than 10 nm.

We conclude that the undulations illustrated in Fig. 16 may be interpreted as a feature of a moving crack in an elastic medium rather than a feature dominated by ductile tearing at the crack tip. Such a crack must satisfy the geometrical rules described elsewhere

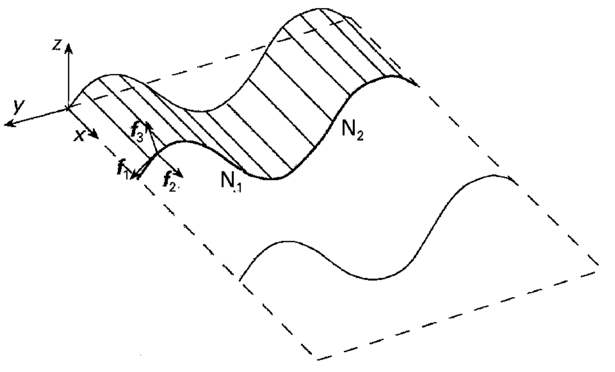

Figure 17 Geometry of a crack on a corrugated surface.

[32] which means that a crack can tilt (rotation about f_3) but not twist (rotation about f_2). Suppose, for simplicity, that a crack lies on a corrugated surface (Fig. 17). There are no geometrical constraints to the growth of the crack on this surface provided that the crack tip remains in the y–z plane. An applied stress in the z-direction produces a mode I opening force where the plane of the crack is normal to the z-axis, and a mixed mode I/III force elsewhere. The maximum rotations of the principal stress field, ϕ, from the z-axis, i.e. the direction of the applied stress, is at points N_1 and N_2 and are of opposite sign. Sommer [36] demonstrated that river lines are nucleated at a critical value $\phi = \phi_c$ and suggested that ϕ_c was a material-related parameter. He reported a value of $\phi_c = 3.3°$ for an inorganic glass. Hull [37] repeated Sommer's work on the same organic glass used in the present work and also found that river lines were nucleated at a critical value of ϕ. In this case it was not possible to measure ϕ_c but the observations suggested that it was smaller than in the inorganic glass used by Sommer.

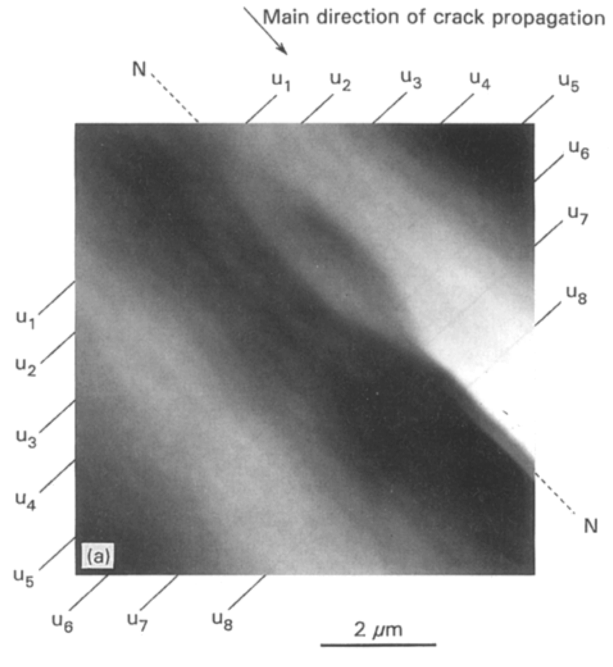

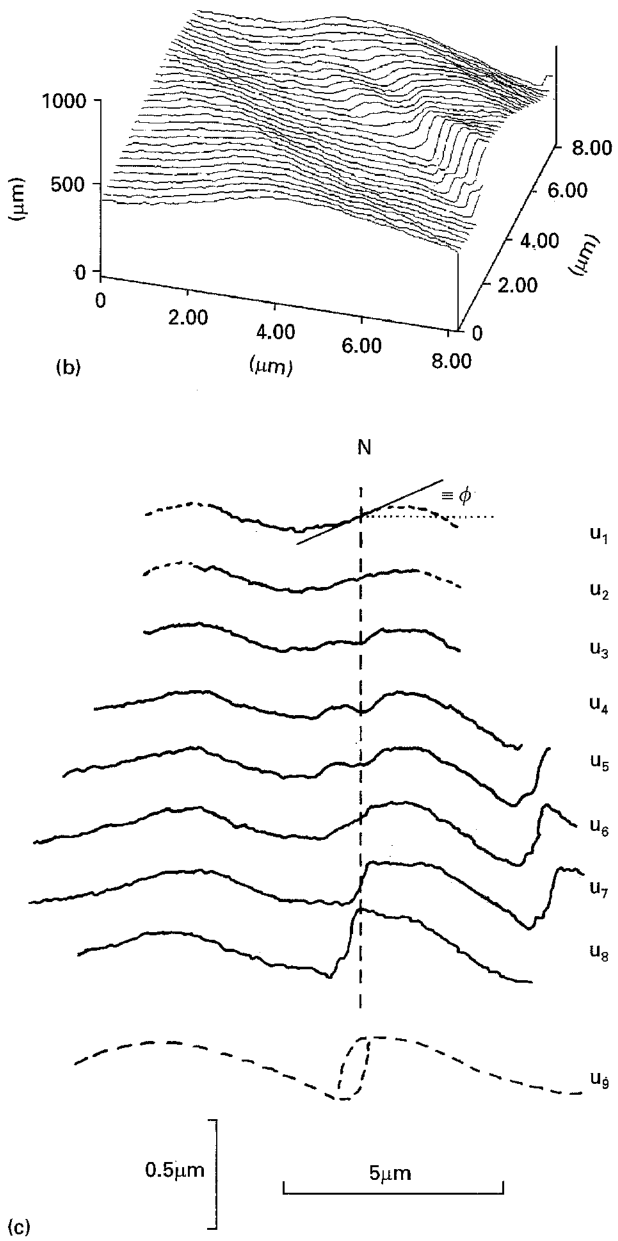

Figure 18 Initiation of river line steps: (a) AFM top surface image; (b) AFM line profile image in the same orientation as (a); (c) line profiles of sections normal to steps and the direction of crack propagation at positions u_1–u_8 marked on (a). u_9 is a schematic profile of a section showing a filament formed by overlapping cracks.

The actual sequence of crack movements leading to the development of undulations and the nucleation of steps has not been determined. However, close examination of the undulations just before nucleation using optical microscopy, SEM and AFM shows that a very distinct process is involved which is illustrated by the experimental results shown in Fig. 18. Fig. 18a is a high-resolution AFM image of the top surface view of the formation of a step (note that the contrast in top surface viewing is achieved by difference in height rather than by shadow contrast effects usually associated with optical and scanning electron microscopy). A characteristic semi-elliptical or fork-shaped topographical feature develops before the formation of the step. A line profile image in the same orientation as Fig. 18a is shown in Fig. 18b and a set of profiles taken normal to the direction of the step is shown in

Fig. 18c. The initial undulations at u_1 resemble the corrugated surface in Fig. 17. The forked feature initiates in the region of maximum slope at N and eventually a step with two overlapping cracks, illustrated in schematic form by u_9, develops in the same region of the undulations. The angle of rotation, ϕ, of the surface at N, measured from the profile, is of the order of 2.5°. The effect of the fold-type instability demonstrated in Fig. 18c is that at the stage represented in u_8 the crack is on two levels. From the evidence presented previously [37] it is clear that the crack fronts bow out on each side and then overlap to produce the filament of separated material.

We know of no theoretical treatment of the progressive development of random fracture surface topography described in this paper although we note the similarity between the development of the instabilities which produce discreet surface steps and the breakdown of laminar flows in fluids. The treatment of Rice *et al.* [41] is probably the most relevant but it is concerned primarily with modelling dynamic propagation of a planar crack under conditions where heterogeneity leads to different local crack velocities in the plane and hence curved crack fronts. Interestingly, they offer an explanation for roughening by arguing that at some positions on the crack front the velocity reaches $v_c = 0.6v_t$ so that it locally satisfies the Yoffe condition [22] for bifurcation. The effects described here are in a significantly lower velocity range. As will be demonstrated in the second paper, after the onset of mist the surface roughening increases progressively as the crack velocity and K_d increase and the mechanisms for out-of-plane crack growth required to explain the observed roughening are extensions of those described in this paper and do not involve the type of microcrack initiation envisaged by, for example, Ravi-Chandar and Knauss [16].

Acknowledgements

The author acknowledges the valuable help with Rodenstock profilometry from Dr Glyn Roper, Shell Thornton Research Laboratories, with atomic force microscopy from Dr Arthur Green, Liverpool University, and with scanning electron microscopy from Dr Peter Beahan, Liverpool University. Professors Peter Goodhew and David Bacon and their colleagues are thanked for generously allowing the author to work in their Department at Liverpool University.

References

1. W. J. JOHNSON and D. G. HOLLOWAY, *Philos. Mag.* **14** (1966) 731.
2. R. W. RICE, in "Fractography of Metal and Ceramic Failures", *ASTM STP* 827, edited by J. J. Mecholsky and S. R. Powell (American Society for Testing and Materials, Philadelphia, PA, 1984) pp. 5–103.
3. B. R. LAWN, "Fracture of Brittle Solids", 2nd Edn (Cambridge University Press, Cambridge, 1993).
4. D. BAHAT, "Tectonofractography" (Springer, Berlin, 1991).
5. H. P. KIRCHNER and J. W. KIRCHNER, *J. Am. Ceram. Soc.* **62** (1979) 198.
6. H. P. KIRCHNER and J. C. CONWAY, *ibid.* **70** (1987) 413.
7. *idem, ibid.* **70** (1987) 419.
8. D. K. SHETTY, G. K. BANSAL, A. R. ROSENFIELD and W. H. DUCKWORTH, *ibid.* **63** (1983) 106.
9. D. HULL and P. BEARDMORE, in "Proceedings of the First International Conference of Fracture", edited by T. Yokobori, T. Kawasaki and J. L. Swedlow (Japan Society for Strength and Fracture of Materials, Sendai, 1966) Vol. 2, pp. 629–45.
10. Y. L. TSAI and J. J. MECHOLSKY, *Int. J. Fract.* **57** (1992) 167.
11. A. S. KOBAYASHI, B. G. WADE, in "Deformation and fracture of high polymers," edited by H. H. Kausch, J. A. Hassell and R. I. Jaffee (Plenum Press, New York, London, 1973) pp. 487–500.
12. J. W. DALLY, W. L. FOURNEY and G. R. IRWIN, *Int. J. Fract.* **27** (1985) 159.
13. J. F. KALTHOFF, *ibid.* **27** (1985) 277.
14. K. RAVI-CHANDAR and W. G. KNAUSS, *ibid.* **25** (1984) 247.
15. *Idem, ibid.* **26** (1984) 65.
16. *Idem, ibid.* **26** (1984) 141.
17. *Idem, ibid.* **26** (1984) 189.
18. K. TAKAHASHI and K. ARAKAWA, *Exp. Mech.* **44** (1987) 195.
19. K. ARAKAWA and K. TAKAHASHI, *Int. J. Fract.* **48** (1991) 103.
20. J. E. FIELD, *Contemp. Phys.* **12** (1971) 1.
21. J. CONGLETON and N. J. PETCH, *Philos. Mag.* **16** (1967) 749.
22. E. H. YOFFE, *ibid.* **42** (1951) 739.
23. L. B. FREUND, "Dynamic fracture mechanics" (Cambridge University Press, Cambridge, 1990).
24. W. J. JOHNSON and D. G. HOLLOWAY, *Philos. Mag.* **17** (1968) 899.
25. D. HULL, (1996) in preparation.
26. *Idem, Int. J. Fract.* **66** (1994) 295.
27. A. J. KINLOCH, S. J. SHAW, D. A. TOD and D. L. HUNSTON, *Polymer* **24** (1983) 1341.
28. "Annual ASTM Standards" (ASTM, Philadelphia, PA 1983) pp. 686–710.
29. P. S. LEEVERS, *J. Mater. Sci.* **17** (1982) 2469.
30. B. STALDER and H. H. KAUSCH, *ibid.* **17** (1982) 2481.
31. S. YAMINI and R. J. YOUNG, *Polymer* **18** (1977) 1075.
32. D. HULL, Int. J. Fract. **62** (1993) 119.
33. H. WALLNER, *Z. Phys.* **114** (1939) 368.
34. A. SMEKAL, *Glastechn. Ber.* **23** (1950) 57.
35. J. H. GREENWOOD, *J. Mater. Sci.* **6** (1971) 390.
36. E. SOMMER, *Eng. Fract. Mech.* **1** (1969) 539.
37. D. HULL, *Int. J. Fract.* **70** (1995) 59.
38. Z. V. DJORDJEVIC, X. FENG LI, W. S. SHIM, S. L. WUNDER and G. R. BARAN, *J. Mater. Sci.* **30** (1995) 2968.
39. D. HULL, *J. Mater. Sci. Lett.* (1996) accepted.
40. C. DE FREMINVILLE, *Rev. Metall.* **11** (1914) 971.
41. J. R. RICE, Y. BEN-ZION and K.-S. KIM, *J. Mech. Phys. Solids* **42** (1994) 813.

Received 9 August
and accepted 8 September 1995